Eur. Phys. J. D **37**, 115–122 (2006)
DOI: 10.1140/epjd/e2005-00278-2

THE EUROPEAN PHYSICAL JOURNAL D

Study of a positive corona discharge in argon at different pressures

R. Benocci[1,a], M. Urbano[2], and L. Mauri[2]

[1] Università degli Studi di Milano-Bicocca, Dipartimento di Fisica "G. Occhialini", P.zza della Scienza 3, 20126 Milano, Italy
[2] SAES Getters S.p.A., Viale Italia 77, 20020 Lainate, Milano, Italy

Received 22 December 2005 / Received in final form 1st August 2005
Published online 25 October 2005 –

Abstract. The corona discharge in argon at atmospheric pressure has been studied by means of a 2D model. The reduced characteristic derived from the experimental data has been described by linear regressions for the different pressures and the two studied inter-electrode distances thus confirming the validity of Townsend's approximation also in case of point to plane configuration and argon as process gas. The model validated this hypothesis which has been attributed to the minor influence of space charge in the ionization zone. Its effect is, on the other hand, more significant in the drift zone where the electric field is greatly enhanced, leading, for higher currents, to the formation of a spark gap. Electron and ion distributions allow the influence of structural (electrode configurations and distance) and operative (pressure and discharge current) parameters to be evaluated including the current loss due to diffusion through different confining boundaries.

PACS. 52.80.Hc Glow; corona

1 Introduction

A corona discharge is characterized by a highly non-uniform electric field due to the small dimensions of at least one electrode (for example a sharp edge or a thin wire) [1,2]. The electric field has very high values in its proximity (active electrode), $E \approx 10^7$ Vm^{-1}, whereas in the remaining gap it is a few orders of magnitude lower: $E \approx 10^4$–10^5 Vm^{-1}. Typical electrode configurations employed in experimental apparatus allowing for this field strength are: point-to-point, point-to-plate, coaxial cylinders with radius r and R ($r \ll R$), parallel thin wires.

The corona discharge has been the object of many studies remarking different discharge features according to the process gas, the polarity of the corona and its steady or pulsed mode of operation [3,4]; the influence of electrode geometry and gas flow rate in air [5,6] and Nitrogen [7]; the influence of chamber temperature [8]; ion mobility measurements [9]; optical emissions [10]; positive corona discharge in gas mixtures [11,12], photocurrents produced by a helium corona [13] and recently in the removal of toxic components from industrial flue gases [14,15].

Numerous numerical models of corona discharge have been proposed. In references [16,17] a wire-to-cylinder corona discharge is modeled. Further refinements of the model include a radial temperature gradient [18]. Recent papers have focused on positive [19] and negative [20] DC coaxial corona discharge. Others have been mostly addressed to glow corona in air [21] and nitrogen [22] both in positive and negative pulsed mode. Usually the 1D modeling has been employed without making allowances for geometric effects. This approach tends to ignore or consider negligible phenomenon such as charged particles distribution, radial losses of charges, estimations of different current contribution to Faraday's cup detectors. In addition to this effect, the influence of electrodes geometry, the electric field distribution and the presence of a flow pattern can be studied more realistically using a 2D approach. In the present paper a 2D model has been adopted to describe a positive corona in argon in a needle-plate configuration. The transport equation for the charged particles and the Poisson's equation have been solved adapting and exploiting the features of a commercial multi-physics tool, disclosing the possibility to model a corona discharge in applied and engineering problems. The numerical results have been tested against the experimental data obtained for different discharge currents, gas pressures and electrode gap distances.

2 Experimental set-up

A point-to-plate electrode has been adopted for the present experiment. A nickel-plated steel needle with a curvature radius $r \approx 25\,\mu$m and a stainless-steel plate of 10 mm diameter have been employed as anode and cathode respectively. The distance between the electrodes, that

[a] e-mail: roberto.benocci@mib.infn.it

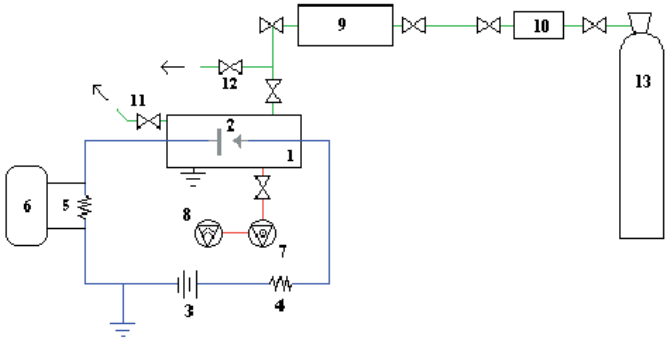

Fig. 1. Experimental set-up.

is regulated through a bellows, has been set to 1 mm and 2 mm.

The corona discharge is ignited, as illustrated in Figure 1, inside a closed cylindrical chamber (diameter 35 mm and length 200 mm) (**1**). The chemically pure argon (99.999%) (**11**), is passed through a mass flow controller (**10**) and a gas purifier (**9**) which reduces its impurity content (O_2, CO, CO_2, H_2, H_2O) to 1 ppb level. During the system warm-up period, the outlet gas is vented through a purge line (**12**). After this stage, the argon flows into the corona chamber. The argon pressure in the chamber has been varied between 1×10^5 and 1.54×10^5 Pa.

The chamber is also joined to a vacuum system including a turbomolecular pump (**7**) and a dry rotary pump (**8**). The system is evacuated, before each experimental measurement, to maintain the chamber and the electrode surfaces clean. A Leybold Membranovac gauge is used to monitor the pressure in the chamber. The power supply (**3**) is a DC high voltage source offering up to 6 kV. The load resistance (**4**) is $R = 100$ MΩ with a current intensity ranging from about 1 to 8 μA. Corona currents are recorded, at the ends of a resistance (**5**) $R = 10$ kΩ, using a LeCroy 9304 AM oscilloscope (**6**).

3 Characteristics

The well-known Townsend's equation [4] is generally employed to describe the $I - V$ characteristic in air in a coaxial wire cylinder geometry:

$$I = kV(V - V_0) \quad (1)$$

where I is the corona current, V the applied voltage, V_0 the initial corona voltage and k a dimensional constant depending on geometrical parameters and the charge carrier mobility (μ) in the drift zone of the discharge. Equation (1) has been derived under the approximation that the space charge does not affect the electric field in the ionization zone.

The currents associated with the positive corona in argon in the present work range between $I \approx 1$–8 μA and are stationary. For higher currents the corona turns into a spark.

Table 1. Regression coefficients of reduced characteristic for an inter-electrode distance of 1 mm.

Pressure (Pa)	K (A/V^2)	V_0 (V)	R^2
1×10^5	5.2113×10^6	889	0.9994
1.04×10^5	5.0094×10^6	878	0.9977
1.20×10^5	4.6175×10^6	962	0.9998

Table 2. Regression coefficients of reduced characteristic for an inter-electrode distance of 2 mm.

Pressure (Pa)	K (A/V^2)	V_0 (V)	R^2
1×10^5	2.0005×10^6	1071	0.9999
1.04×10^5	2.0008×10^6	1042	0.9998
1.20×10^5	1.6758×10^6	1098	0.9997
1.35×10^5	1.5287×10^6	1254	0.9976
1.54×10^5	1.3091×10^6	1282	0.9998

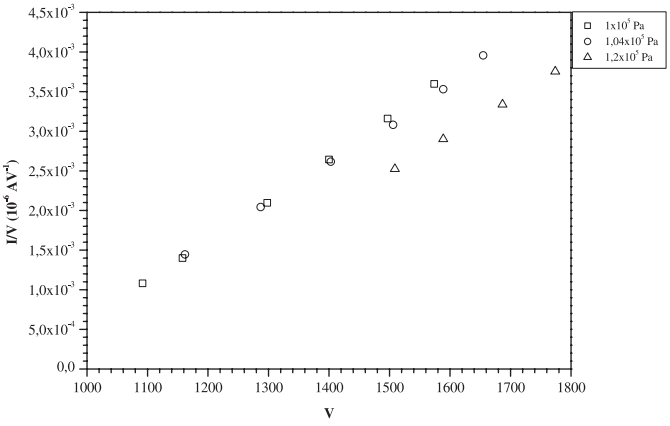

Fig. 2. I/V characteristic at different chamber pressure, $d =$ 1 mm.

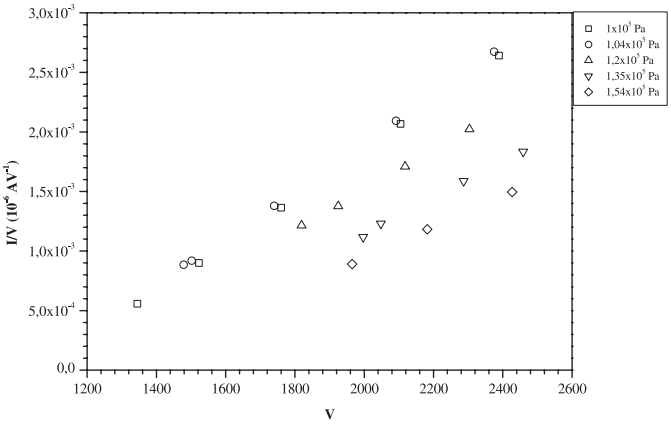

Fig. 3. I/V characteristic at different chamber pressure, $d =$ 2 mm.

The reduced characteristic, I/V vs. V, derived from the experimental data can be described, with fair agreement, by linear regressions for the different pressures and the two studied inter-electrode distances as shown in Tables 1 and 2 and Figures 2 and 3. This means that in the studied case, the validity of equation (1) can be extended,

Table 3. Boundary conditions.

	1	2	3	4	5
n_e	$\underline{n\Gamma}_e = 0$	$\underline{n\Gamma}_e = \gamma\,\underline{n\Gamma}_i$	$n_e = 0$ [23]	$\underline{n\Gamma}_e = 0$	$\frac{\partial n_e}{\partial n} = 0^{(*)}$
n_i	$\underline{n\Gamma}_i = 0$	$\frac{\partial n_i}{\partial n} = 0$	$n_i = 0$ [23]	$\underline{n\Gamma}_i = 0$	$n_i = 0$
V	$\frac{\partial V}{\partial n} = 0$	$V = V_C$	$\frac{\partial V}{\partial n} = 0$	$\frac{\partial V}{\partial n} = 0$	$V = V_A$

$^{(*)}\partial/\partial n$ normal derivative with respect to surface.

with good degree, also to the positive corona in argon in point to plane configuration.

The linear regression coefficients k and V_0 depend on the gas pressure increase in the chamber. According to Paschen's law, the initial corona voltage V_0 increases as the pressure rises, for a fixed electrode distance. Instead, for a given pressure, V_0 is higher when the electrode distance is 2 mm. The angular coefficient of the linear regression k decreases as the pressure goes up. This fact can be explained considering that k is proportional to the ion mobility μ_i, this latter being inversely proportional to the pressure: $k \propto \mu_i \propto 1/p$ [24].

The linear regression coefficients, corresponding to the pressure value 1.04×10^5 Pa, represent an exception to the described behavior. The I/V-V characteristic is almost identical to the curve corresponding to the pressure value $1{\times}10^5$ Pa, as shown in Figures 2 and 3. In this case, the small pressure difference is not sufficient to clearly separate the corresponding characteristics.

The effect of pressure variation has been taken into account by correlating the pressure increase in the chamber to the measured argon gas flow rate, as shown in Figure 4; charged species transport due to gas convection has been neglected. The gas has been chosen to flow parallel to ions drift motion (from tip to plate). The discharge characteristic presents a significant dependence of the current on the argon pressure resulting in a low discharge current as the pressure is increased.

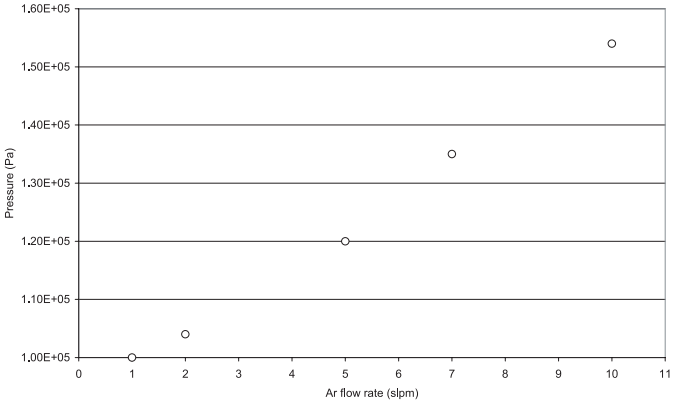

Fig. 4. Pressure increase as a function of argon gas flow rate.

4 Corona model

For the mathematical description of the positive corona discharge, the transport equation for electrons and ions, together with the Poisson's equation for the electric field have been used. As source term in the electron and ion equation, the Townsend's formula has been considered. The equations are:

$$\nabla \cdot (D_e \nabla n_e + \mu_e \underline{E} n_e) = -\alpha n_e \left|\underline{u}_e\right| \tag{2}$$

$$\nabla \cdot (D_i \nabla n_i - \mu_i \underline{E}\, n_i) = -\alpha n_e \left|\underline{u}_e\right| \tag{3}$$

$$\nabla \cdot \underline{E} = \frac{1}{\varepsilon_0} e\,(n_i - n_e) \tag{4}$$

where n_e and n_i are the electron and ion densities; μ_e, D_e, μ_i and D_i are the mobility and diffusion coefficient for electrons and ions; $\underline{u}_e$ is the electron drift velocity; α is the ionization coefficient given by:

$$\alpha = Ap\, e^{\frac{-Bp}{E}} \tag{5}$$

where A and B are coefficients proper of the specific gas; p is the chamber pressure; $\underline{E}$ is the electric field and E its modulus. In equations (2, 3) the recombination term has been omitted being many orders smaller than the ionization term.

Zero density for ions and pure convective flux for electrons boundary conditions are imposed at the anode. Pure convective flow for ions is set at the cathode whereas, at the anode, the electron current density,

$$\underline{\Gamma}_e = -D_e \nabla n_e - \mu_e \underline{E} n_e$$

is maintained proportional to the ion current density, Γ_i, according to the following relation

$$\underline{n\Gamma}_e = -\gamma\, \underline{n\Gamma}_i. \tag{6}$$

The constant of proportionality γ accounts for secondary electron emission by ion impact, electron emission from the electrodes by UV radiation generated in the discharge and by metastable atoms impinging on the electrodes, $\underline{n}$ is the normal vector to the surface. In Table 3 the boundary conditions adopted for the solution of the set of equations (2–4) are listed, referring to Figure 5 for the calculation domain.

The conditions on boundaries 3 and 4 are worth some comments: the problem domain, in fact, should in principle comprehend the whole chamber; in order to reduce the calculation domain, virtual boundary 3 and 4 have been placed sufficiently far from the needle tip as to minimally affect the discharge: symmetry conditions have been set on these boundaries for the electric field. Furthermore, in order to have non-zero ion current, zero ion density condition has been set on boundary 3. The radial distribution

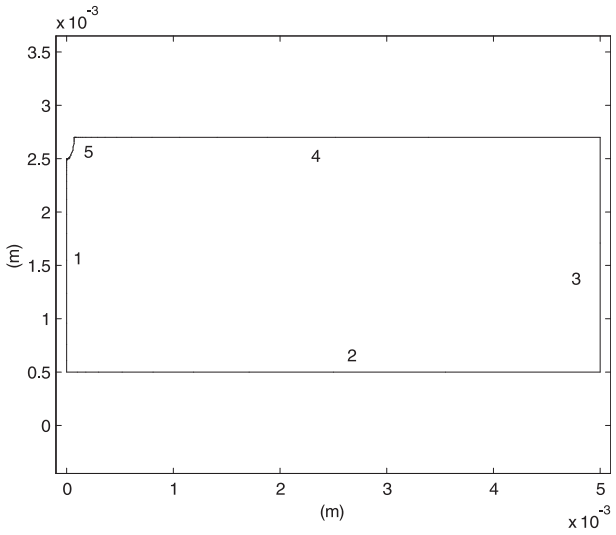

Fig. 5. Scheme of calculation domain.

Table 4. Parameters used in equations (2–4) [24].

Quantity	Units
$\mu_i p$	19 $m^2V^{-1}s^{-1}$ Pa
$\mu_e p$	$4.4 \times 10^3 m^2V^{-1}s^{-1}$ Pa
$D_e p$	8.4×10^3 Pa m^2s^{-1}
$D_i p$	0.5 Pa m^2s^{-1}
γ	1.1×10^{-4}
A	9 m^{-1} Pa^{-1}
B	135 Vm^{-1} Pa^{-1}

of ion density computed at the anode confirms that the discharge takes place in a region inside the reduced domain.

The parameters used in the equations are summarized in Table 4. The ion diffusion coefficient has been computed according to the Einstein's relation at a temperature of 300 K. The value of γ has been fitted so that, for a gap distance of 1 mm, the computed current at 1100 V matches the experimental value of 1.2 μA.

Mobility and diffusion parameters are considered constant throughout the whole discharge region. This is a simplification as they depend on the gas and electron temperature; moreover, ion mobility is affected by ion molecule reactions like $Ar^+ + 2Ar \rightarrow Ar_2^+ + Ar$ taking place in the gap region. This reaction represents the most probable reaction in UHP argon, whose reaction rate constant is $K = 4.4 \times 10^{-43}\,m^6/s$ [25]. The average Ar^+ lifetime can be estimated with the following equations:

$$\frac{dn^{Ar^+}}{dt} = -n^{Ar^+} n^2 K, \quad \frac{dn^{Ar_2^+}}{dt} = n^{Ar^+} n^2 K$$
$$n^{Ar^+} = n_0^{Ar^+} e^{-Kn^2 t} \tag{7}$$

where n is the neutral gas density. The Ar^+ lifetime turns out to be of about 10^{-8} s (n is about $2 \times 10^{25}\,m^{-3}$ in standard condition). During this period of time ions travel a distance of 2×10^{-5} m in presence of an electric field of 10^7 V/m and 2×10^{-6} m with a field of 10^6 V/m. This means that most of the inter-electrode gap is populated by Ar_2^+ ions.

Equations (2–4) have been solved iteratively by setting a positive electric potential, V_A, at the anode and grounding the cathode, $V_C = 0$ V.

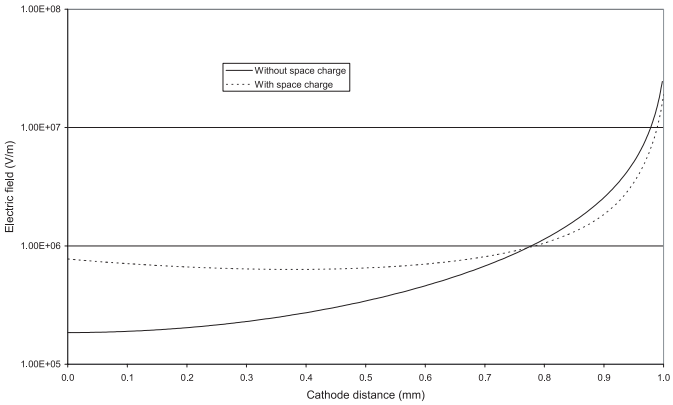

Fig. 6. Electric field intensity along the symmetry axis with and without space charge: $V = 1200$ V, $I = 1.9$ μA, $P = 10^5$ Pa.

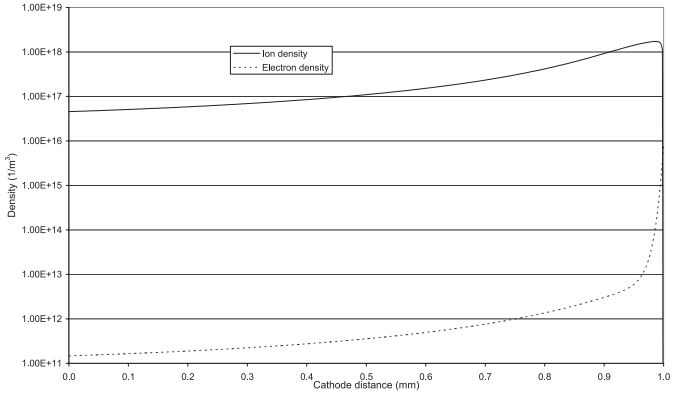

Fig. 7. Ion and electron density distribution along the symmetry axis: $V = 1200$ V, $I = 1.9$ μA, $P = 10^5$ Pa.

5 Discussion of results

A needle electrode with a tip radius of 25 μm placed at a distance of a few millimeters from a plane electrode creates steep electric field gradients close to the tip. For this reason, an adapted grid with elements dimension ranging from 10^{-7} m to 10^{-6} m has been employed.

The gap between the electrodes can be divided into two separate regions: a region close to the needle where ionization processes take place, and a drift region where practically only ions are present. The first region is characterized by a high electron density (10^{14}–$10^{16}\,m^{-3}$) and a strong electric field (10^7 V/m). In the drift region, on the contrary, the electron density and the electric field go down to values of 10^{10}–$10^{13}\,m^{-3}$ and 10^5–10^6 V/m (see Figs. 6 and 7). The ion density presents a maximum in the ionization region ($\approx 10^{18}\,m^{-3}$) reducing of about one

order of magnitude in the drift region. The effect of space charge can be appreciated by comparing the electric field with and without its influence (see Fig. 6): in the ionization region the electric field intensity is slightly lowered by the space charge passing from $E_{max} = 2.5 \times 10^7$ V/m to $E_{max_{sc}} = 1.9 \times 10^7$ V/m for a corona current of 1.9 μA. This effect can thus be associated with a mild stabilizing effect on the ionizing process. However this result does not contradict the assumption that the space charge does not affect significantly the electric field in the ionization zone (Townsend's approximation). On the other hand, major effects are evident in the drift region: the electric field increase is more marked passing from $E_{min} = 1.85 \times 10^5$ V/m to $E_{min_{sc}} = 6.33 \times 10^5$ V/m; the space charge effect, in this case, tends to increase the electric field and thus to intensify the ionization process. If this phenomenon is protracted at higher currents the corona turns into a spark (see Fig. 16).

In Figures 8 and 9 the spatial distribution of electrons and ions is illustrated. Electrons are concentrated in the narrow ionization region close to the tip. In the same region the ion cloud is generated and spreads sensibly towards the cathode. The spreading is mainly due to diffusion phenomena. Figures 10 and 11 show a fairly good agreement between computed and experimental I-V characteristics. In particular the variations of the I-V characteristic with pressure and distance are quite well reproduced. Computed currents are slightly overestimated for a gap distance of 2 mm. The general behavior of the characteristic quantities of the discharge can be summarized as follows: electron and ion densities increase raising the applied potential, V, as a result of the higher electric field, E, and thus of the ionization coefficient growth, α (see Figs. 12 and 13); In particular, the electron density in the ionization region changes from $n_{e_{max_{1100}}} = 8.5 \times 10^{15}\,\mathrm{m}^{-3}$ to $n_{e_{max_{1900}}} = 3 \times 10^{16}\,\mathrm{m}^{-3}$ for an applied voltage passing from 1100 V to 1900 V, whereas in the cathode proximity $n_{e_{max_{1100}}} = 1.2 \times 10^{11}\,\mathrm{m}^{-3}$ goes up to $n_{e_{max_{1900}}} = 3.2 \times 10^{11}\,\mathrm{m}^{-3}$; for the ion density $n_{i_{max_{1100}}} = 1.6 \times 10^{18}\,\mathrm{m}^{-3}$ becomes $n_{i_{max_{1900}}} = 5.5 \times 10^{18}\,\mathrm{m}^{-3}$ and $n_{i_{max_{1100}}} = 3.5 \times 10^{16}\,\mathrm{m}^{-3}$ $n_{i_{max_{1900}}} = 9 \times 10^{16}\,\mathrm{m}^{-3}$ for the same regions; for the electric field $E_{max_{1100}} = 1.91 \times 10^7$ V/m gets to $E_{max_{1900}} = 1.66 \times 10^7$ V/m in the first region and from $E_{max_{1100}} = 6.4 \times 10^5$ V/m to $E_{max_{1900}} = 1.7 \times 10^6$ V/m in the second (see Fig. 16) due to space charge effects. Figures 14 and 15 show the radial distribution of electrons and ions at the cathode plate for different applied potentials. It can be observed that for identical discharge current $I = 1.2$ μA, both charged particles densities and the electric field increase with increasing the pressure as illustrated in Figures 17 and 18 for two inter-electrode distance: 1 and 2 mm. In this case, the reduction of the ionization coefficient α due to the pressure increment (see Eq. (5)) is more than compensated by the higher voltage required to sustain the imposed current. In fact, for an inter-electrode distance of 2 mm and a current $I = 1.2$ μA, α_{max} grows from $\alpha_{max_{P_0}} = 4.5 \times 10^5$ m^{-1} at $P_0 = 10^5$ Pa and an applied potential of $V_0 = 1400$ V (in Eq. (5) E_{max} has been

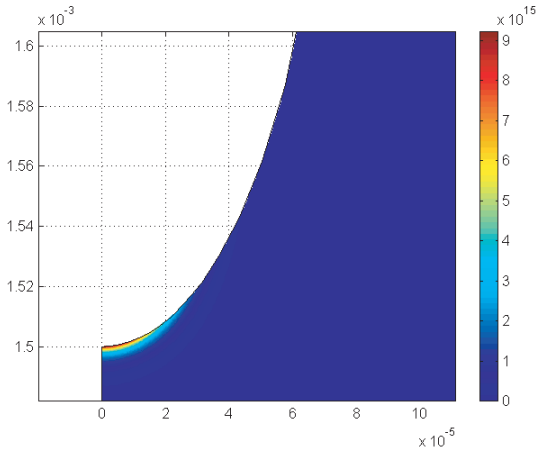

Fig. 8. Distribution of electron density close to the needle tip: $V = 1200$ V, $I = 1.9$ μA, $P = 10^5$ Pa. A color version of the figure is available in electronic form at `http//www.eurphysj.org`.

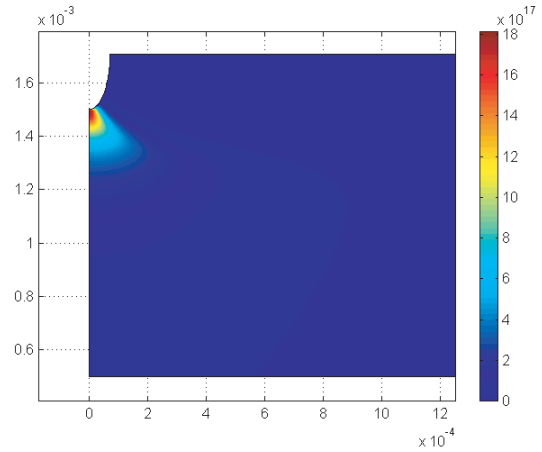

Fig. 9. Distribution of ion density: the region close to the needle tip is represented, $V = 1200$ V, $I = 1.9$ μA, $P = 10^5$ Pa. A color version of the figure is available in electronic form at `http//www.eurphysj.org`.

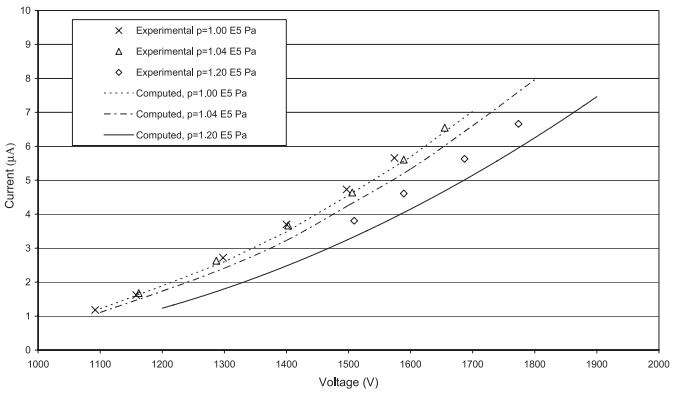

Fig. 10. Comparison between experimental and computed I-V characteristic; $d = 1$ mm.

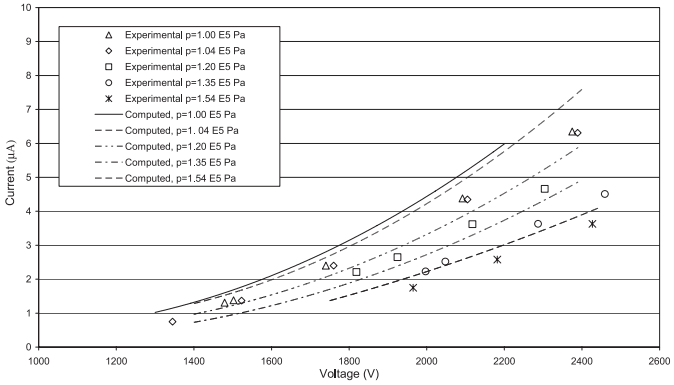

Fig. 11. Comparison between experimental and computed I-V characteristic; $d = 2$ mm.

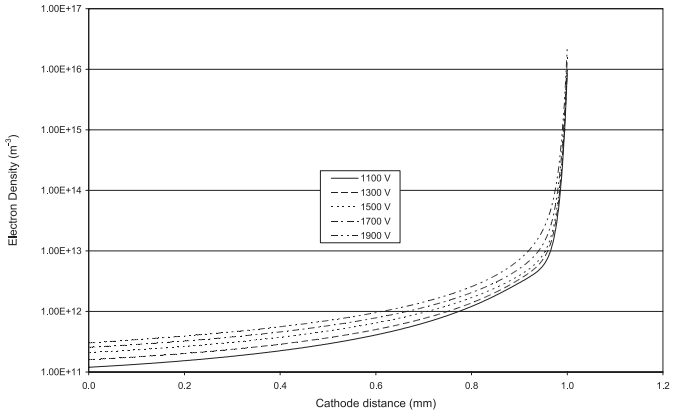

Fig. 12. Electron density along symmetry axes for different applied voltages; $d = 1$ mm, $P = 10^5$ Pa.

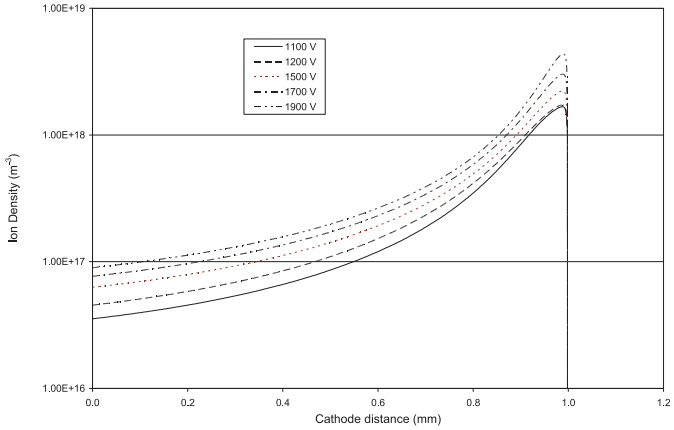

Fig. 13. Ion density along symmetry axes for different applied voltages; $d = 1$ mm, $P = 10^5$ Pa.

considered) to $\alpha_{max_{P_1}} = 5.5 \times 10^5$ m^{-1} at $P_1 = 1.5 \times 10^5$ Pa and an applied potential of $V_1 = 1750$ V.

As it can be expected, the ion cloud at the cathode plate becomes wider for higher gap distance (see Fig. 19). In this case, the effect of a more pronounced diffusion can be estimated calculating the current loss due to diffusion across side 3 of Figure 5. For a fixed value of corona current $I = 2.6$ μA the calculated drift current due to diffusion is

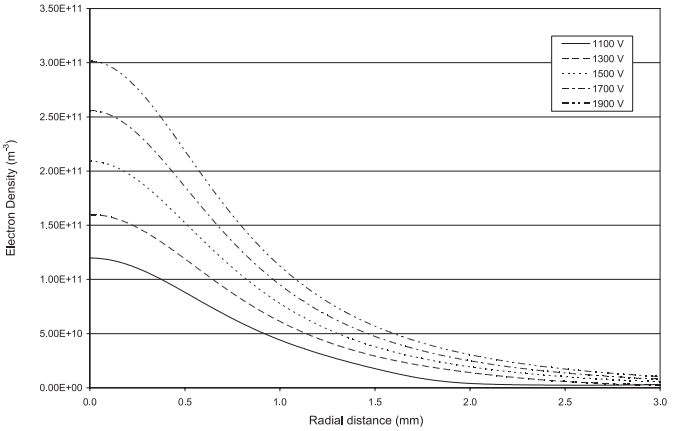

Fig. 14. Radial electron density distribution at the cathode plate; $d = 1$ mm, $P = 10^5$ Pa.

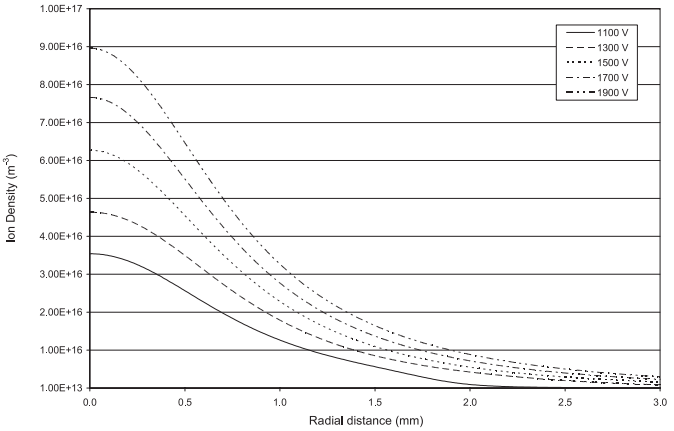

Fig. 15. Radial ion density distribution at the cathode plate; $d = 1$ mm, $P = 10^5$ Pa.

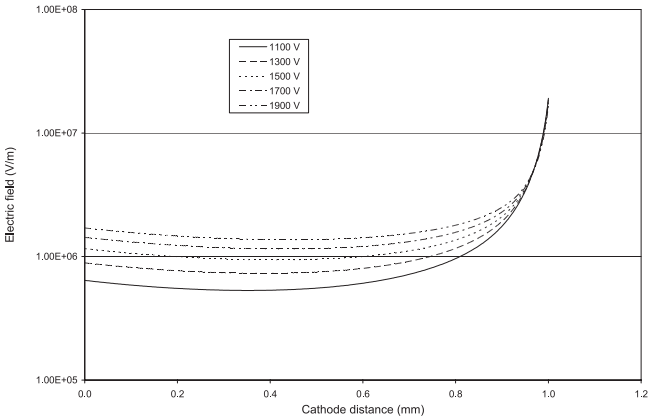

Fig. 16. Electric field along symmetry axes for different applied voltages; $d = 1$ mm, $P = 10^5$ Pa.

of 1.7×10^{-11} μA and 2.6×10^{-10} A for a gap of 1 and 2 mm respectively.

A comparison has also been made for an inter-electrode distance of 2 mm by changing the boundary condition for the potential on side (3) of Figure 5. In case of $\partial V/\partial n|_3 = 0$, the current lost by diffusion across side (3)

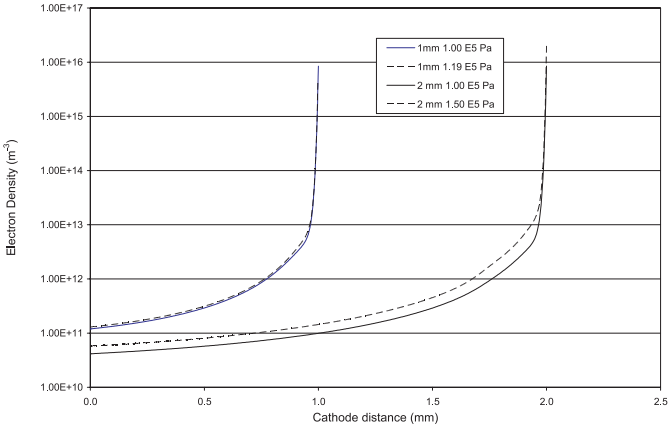

Fig. 17. Electric density along symmetry axes for two different pressures and gap distances, $I = 1.2$ μA.

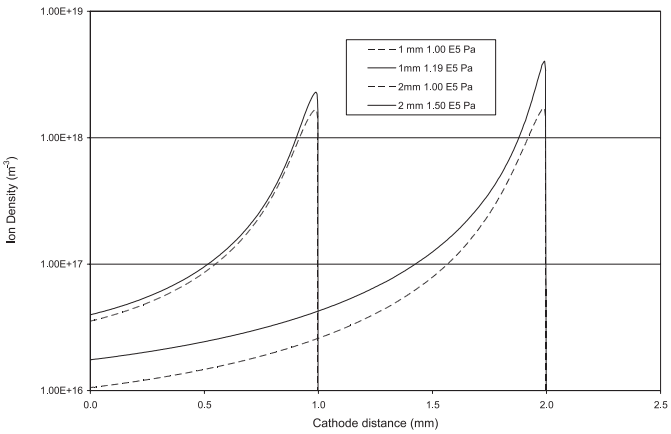

Fig. 18. Ion density along the symmetry axes for two different pressures and gap distances $I = 1.2$ μA.

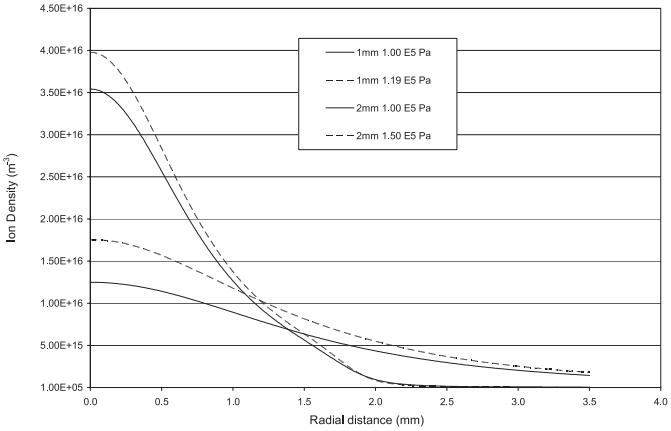

Fig. 19. Radial ion density distribution at the cathode plate for two different pressures and gap distances, $I = 1.2$ μA.

represents the 0.003% of the total discharge current at 1 μA and about 0.014% at 6 μA as illustrated in Figure 20. In case the boundary on side (3) is kept at V_C potential, $\underline{n\Gamma}_e = \gamma \underline{n\Gamma}_i$, and $\partial n_i/\partial n|_3 = 0$, the radial current ranges between about 3 and 6.5% of the total current (see Fig. 21).

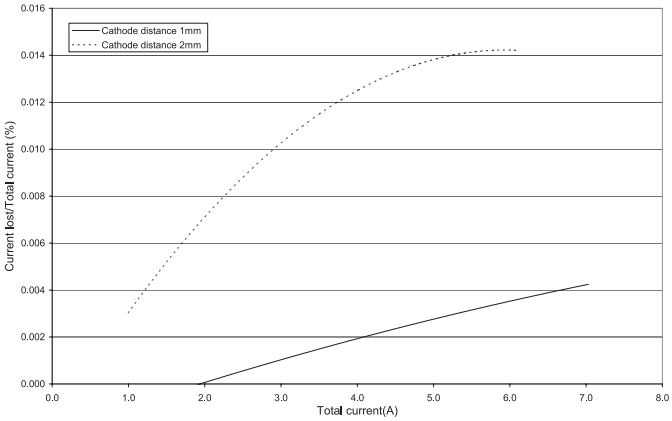

Fig. 20. Radial to total current ratio due to diffusion: $d = 2$ mm, $P = 10^5$ Pa and boundary conditions of Table 3.

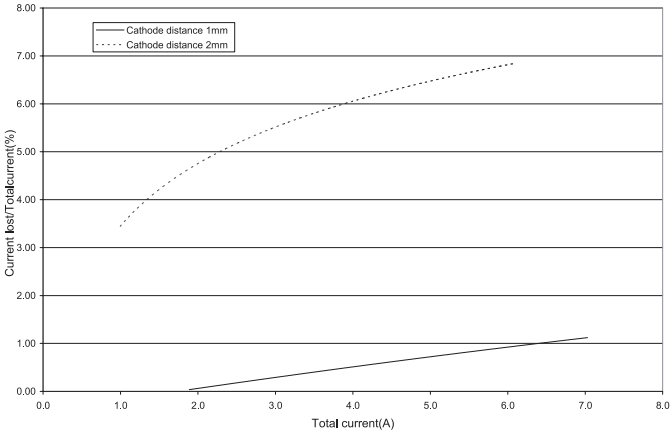

Fig. 21. Radial to total current ratio due to drift and diffusion: $d = 2$ mm, $P = 10^5$ Pa and boundary condition: $V = V_C$, $\Gamma_e = 0$ and $n_i = 0$.

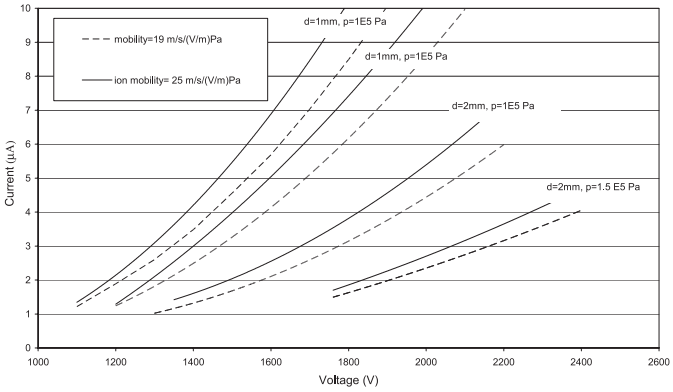

Fig. 22. Effect of mobility on I-V characteristics.

As previously mentioned, constant mobility and diffusion coefficients have been used in the mathematical formulation of the model. In literature different values of argon ion mobility are reported: for example, Von Engel gives values of $\mu_i p$ of 16 $\mathrm{m^2\,V^{-1}\,s^{-1}\,Pa}$ and 26.5 $\mathrm{m^2\,V^{-1}\,s^{-1}\,Pa}$ for Ar^+ and Ar^{2+} respectively [26]. In order to evaluate the influence of variations of ion mobility, the I-V characteristics of the corona discharge have been

calculated for different values of ion mobility (Fig. 22). A higher value of ion mobility produces steeper I-V characteristics. Due to the sensitivity of ion mobility on I-V characteristics, it is reasonable to argue that energy issues can play a role on the general behavior of the discharge: in fact, mobility and diffusion lengths are quantities that depend on charged particles temperature and neutrals temperature and density, these depending ultimately on discharge parameters. These aspects are left for discussion of future papers.

6 Conclusions

The corona discharge in argon at atmospheric pressure has been studied by means of a 2D model.

The reduced characteristic derived by the experimental data has been described, with fair agreement, by linear regressions for the different pressures and the two studied inter-electrode distances thus confirming the validity of Townsend's approximation. This hypothesis has been validated by the model due to the minor influence of space charge in the ionization zone. Its effect is, on the other hand, more significant in the drift zone where the electric field is greatly enhanced, leading, for higher currents, to the formation of a spark gap. Electron and ion distributions allow the influence of structural (electrode configurations and distance) and operative (pressure and discharge current) parameters to be evaluated including the current loss due to diffusion through different confining boundaries.

References

1. M. Faraday, *Experimental Researches in Electricity* (Dover, New York, 1965), Vol. 1, p. 10
2. L.B. Loeb, *Electrical Coronas* (University of California Press, 1965), p. 120
3. Yu.S. Akishev et al., Plasma Phys. Rep. **27**, 520 (2001)
4. Yu.S. Akishev et al., J. Phys. D: Appl. Phys. **32**, 2399 (1999)
5. Yu.S. Akishev et al., J. Phys. D: Appl. Phys. **34**, 2875 (2001)
6. R. Morrow, J. Phys. D: Appl. Phys. **30**, 3099 (1997)
7. R. Benocci, A. Galassi, L. Mauri, M. Piselli, M. Sciascia, Eur. Phys. J. D **25**, 157 (2003)
8. H.S. Uhm, Phys. Plasmas **6**, 623 (1999)
9. R.G. Stearns, J. Appl. Phys. **67**, 2789 (1990)
10. F. Tochikubo et al., Jpn. J. Appl. Phys. **39**, 1343 (2000)
11. A.K. Shuaibov et al., Tech. Phys. **46**, 1582 (2001)
12. K. Hensel et al., Jpn. J. Appl. Phys. **41**, 336 (2002)
13. R. Benocci, L. Mauri, J. Phys. D: Appl. Phys. **37**, 709 (2004)
14. R. Hackam, J.S. Chang, IEEE Trans. Dielectr. Electr. Insul. **7**, 654 (2000)
15. K. Urashima, J.S. Chang, IEEE Trans. Dielectr. Electr. Insul. **7**, 602 (2000)
16. S. Hadj Ziane, B. Held, P. Pignolet, R. Peyrous, J.M. Benas, J. Phys. D: Appl. Phys. **23**, 1390 (1990)
17. S. Hadj Ziane, B. Held, P. Pignolet, R. Peyrous, C. Coste, J. Phys. D: Appl. Phys. **25**, 677 (1992)
18. J.F. Loiseau, F. Lacassie, C. Monge, R. Peyrous, B. Held, J. Phys. D: Appl. Phys. **27**, 63 (1994)
19. J. Chen, J.H. Davidson, Process. **22**, 199 (2002)
20. J. Chen, J.H. Davidson, Process. **22**, 495 (2002)
21. R. Morrow, Phys. Rev A **32**, 1799 (1985)
22. Yu. S. Akishev et al., Plasma Phys. Rep. **27**, 532 (2001)
23. J.R. Lamarsh, *Introduction to Nuclear Reactor Theory* (Addison-Wesley Publishing Company, Reading, 1965)
24. Yu.P. Raizer, Gas discharge Physics (Springler-Verlag, Berlin, 1991)
25. W. McDaniel, V. Čermák, A. Dalgrano, E.E. Ferguson, L. Friedman, *Ion-Molecule reactions* (Wiley-Interscience, 1970)
26. A. Von Engel, *Ionized Gases* (Oxford University Press, Oxford, 1964)